

Ion Transport in Pendant and Backbone Polymerized Ionic Liquids

Preeya Kuray¹, Takeru Noda², Atsushi Matsumoto³, Ciprian Iacob^{4,5}, Tadashi Inoue^{2}, Michael A. Hickner^{1,6,7*}, and James Runt^{1*}*

¹Department of Materials Science and Engineering, The Pennsylvania State University, University Park, PA 16802, USA

²Department of Macromolecular Science, Osaka University, 1-1 Machikaneyama-cho, Toyonaka, Osaka 560-0043, Japan

³Okinawa Institute of Science and Technology Graduate University, Onna, Okinawa 904-0495, Japan

⁴National Research and Development Institute for Cryogenic and Isotopic Technologies, ICSI Rm. Valcea, Romania

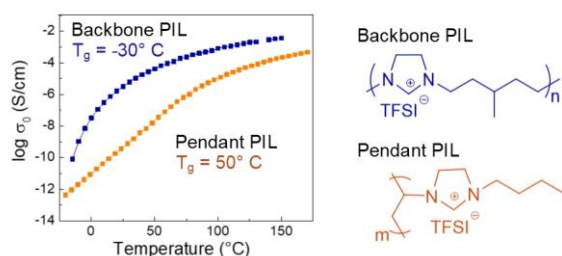
⁵Karlsruhe Institute of Technology (KIT), Institute for Chemical Technology and Polymer Chemistry, 76128, Karlsruhe

⁶Department of Chemical Engineering, The Pennsylvania State University, University Park, PA 16802, USA

⁷Department of Chemistry, The Pennsylvania State University, University Park, PA 16802, USA

*Corresponding Authors: James Runt, jpr1@psu.edu, Michael A. Hickner, mah49@psu.edu, Tadashi Inoue, tadashi@chem.sci.osaka-u.ac.jp

TOC figure



ABSTRACT: Polymerized ionic liquids (PILs) are single-ion conductors in which one of the ionic species is tethered to the polymer chain while the other is free to be transported. The ionic species can either be directly incorporated into the polymeric backbone (backbone PILs) or placed as pendant groups to the chain (pendant PILs). Here, we examined the morphology, conductivity, and rheology of imidazolium-based pendant and backbone PILs. We found that pendant PILs yielded higher ionic conductivity when scaled to T_g , but backbone PILs exhibited higher ionic conductivity on an absolute temperature scale, likely due to differences in the T_g s of the two systems. We also found that ion transport for backbone PILs was coupled to the segmental dynamics even below T_g where the decoupling of ionic conductivity from segmental relaxation was observed for pendant PILs. The results of this study will help the community to better understand the role of PIL structure on conductivity to work towards the ultimate goal of designing high-performance solid polymer electrolytes.

Key Words: Polymerized ionic liquids; dielectric relaxation spectroscopy; charge-transport; ionenes; polyelectrolytes

1. Introduction

Today's ever-growing energy demands and push towards new energy technologies have led to an increased need for improved electrolyte materials in applications such as lithium-ion batteries and dye-sensitized solar cells. Thus far, ionic liquids (ILs) have been used as electrolytes for a variety of electrochemical systems, because of their high conductivity and thermal stability.¹⁻³ However, the leakage issues that are often prevalent with ILs have motivated the search alternative electrolytes. In the past decade, there has been a concerted effort to incorporate ion-conducting polymers into a variety of energy conversion and storage devices due to their mechanical stability and ability to conduct ions in the solid or semi-solid state. Polymerized ionic liquids (PILs) are single ion conductors, in which one of the ionic

species is fixed to the polymer chain while the other (counter-ion) is nominally free to be transported.⁴ In common synthetic designs, the ionic species can either be directly incorporated into the polymeric backbone (ionenes, or backbone PILs) or placed in pendant groups on the side chain (pendant PILs).⁵ At temperatures greater than the glass transition temperature of the material, conductivity in PILs is typically coupled to segmental motion and attained by hopping of counter-ions between ionic sites due to segmental motion of the polymer chain.⁶⁻⁸ However, in order to ultimately serve as a viable solid-state alternative to traditional liquid electrolytes, PILs must also be sufficiently conductive below their respective T_g . Sangoro et al.⁹ have studied conductivity and structural dynamics in pendant imidazolium-based PILs, observing conductivity (10^{-8} S/cm) below the glass transition temperature. In this temperature range, the motion of the polymer chain is “frozen”, and the ion movement is attributed to the continued mobility of the counter-anions from decoupling. Although ion mobility in the solid state below T_g is possible, substantial conductivity needed for practical applications is difficult to achieve without polymer chain segmental movement. Therefore, the fundamental mechanisms required to improve low ion transport rates inherent in glassy polymers and the influence of structure need to be better understood in PILs.

Hall et al.¹⁰ performed early work using molecular dynamic simulations of ionomer melts that compared the scattering peak of ionomer melts with precisely placed charges placed within the polymer chain (ionenes) and pendant to the polymer backbone. Ionenes were found to have a more percolated path for charge transport, attributed to the charges being fixed along the polymer chain whereas pendant-type ionomers were found to form discrete ionic aggregates that hindered ion transport. These aggregates were anticipated to substantially lower ionic conductivity compared to the ionenes, which was confirmed by subsequent experimental studies. Evans et al.⁵ investigated the impact of positioning the charged group along pendant positions and along the organic backbone for PILs. It was found that a backbone PIL (T_g : -35

°C) yielded a ten-fold increase in T_g -normalized ionic conductivity compared to their pendant PIL (T_g : 16 °C), possibly arising from the difference in morphology accompanying the placement of the charged group in the polymer backbone leading to a more percolating pathway for conduction. However, there were polar linkers in the pendant PIL structures of Evans et al., which could have a major influence on the observed conductivities in terms of ion-specific effects outside of T_g effects. Imrie et al.¹¹ compared the conductivities of ethylene oxide-based pendant and backbone polyelectrolytes and found that sub- T_g ionic conductivity arose in the polyelectrolyte samples with pendant groups due to stiffening of the backbone from the addition of the isophthalic ester link units on the side groups. This stiffening prevented the formation of ethylene oxide coils that could potentially trap counter-cations at lower temperatures, inhibiting conductivity.

Research efforts have also been dedicated to mapping and understanding the impact of molecular structure of P-PILs on the ion transport mechanism.^{9,12-26} The ion transport for P-PILs was found to be governed by the cation-anion interaction,²⁷⁻²⁹ chain packing,³⁰⁻³² and counter-ion size.^{33,34} The underlying mechanism of the decoupling behavior has been studied by Sokolov and coworkers. They found that the degree of decoupling increases when increasing the fragility of polymers. Furthermore, Stacy et al.³⁵ have very recently reported that the competition between Coulombic and elastic forces, which depends on the counter-ion size, determines the activation energy for the ion diffusion in the glassy P-PILs. Salas-de la Cruz et al.²² studied PIL structure as a function of alkyl length and temperature using wide-angle X-ray scattering techniques. They found a correlation between backbone-to-backbone distance and ionic conductivity. Counter-ion size is another critical factor in determining ion transport since smaller ions tend to exhibit higher mobility. Iacob et al.³⁴ have found that the size of the counter-anion results in a four orders of magnitude difference in the glass transition independent ionic conductivity for a broad series of imidazolium based pendant PILs. Despite

extensive work on the relationship between morphology and ionic mobility in pendant PILs, there has not yet been a cohesive study on examining how this relationship might change for different polymer chemistries of pendant and backbone PILs, and how the insights of structure may be convoluted with specific ion interactions, segmental mobility, and T_g effects. The objective of the present study is thus to investigate both the impact of PIL chemical structure on the ionic conductivity and relaxation mechanisms of pendant and backbone PILs that are based on imidazolium cations and aliphatic backbones.

We used X-ray scattering to quantify correlation lengths, dielectric relaxation spectroscopy to measure the ionic conductivity and peak relaxation frequencies for ionic motion, as well as rheology to quantify peak relaxation frequencies for segmental motion of backbone and pendant PILs in the amorphous state. We found that pendant PILs yield substantially higher T_g -normalized conductivity compared to their equivalent backbone counterparts, while the backbone PILs under investigation yield higher conductivity on an absolute temperature scale. By comparing dielectric and rheological relaxation frequencies, we have also found that the ion transport for backbone PILs is coupled to the segmental dynamics even below T_g where the decoupling is observed for pendant PILs. The comparisons from this work will assist in developing a deeper understanding of ion transport in PILs and ultimately help pave the way towards maximizing conductivity in next-generation polymer electrolytes.

2. Experimental

Materials

Imidazole, 1,5-dibromo-3-methylpentane, dimethyl sulfoxide (DMSO), lithium bis(trifluoromethanesulfonyl)imide (Li-TFSI), lithium nonafluorobutanesulfonate (Li-NfO), and silver nitrate (AgNO_3) at 0.1 M in an aqueous solution were purchased from Wako Pure Chemicals, Japan. Sodium bicarbonate (NaHCO_3) was purchased from Kishida Chemical Co., Ltd., Japan. Lithium 1,1,2,2,3,3-hexafluoropropane-1,2-disulfonimide (Li-CPFSI) was

purchased from Tokyo Chemical Industry Co., Ltd., Japan. These materials were used as received. Deionized water (DI water) with a specific resistance higher than 16 MΩ-cm was obtained using an Elix system (Japan Millipore, Japan) and used as a pure water.

Synthesis

Backbone/Pendant Polymer Cation

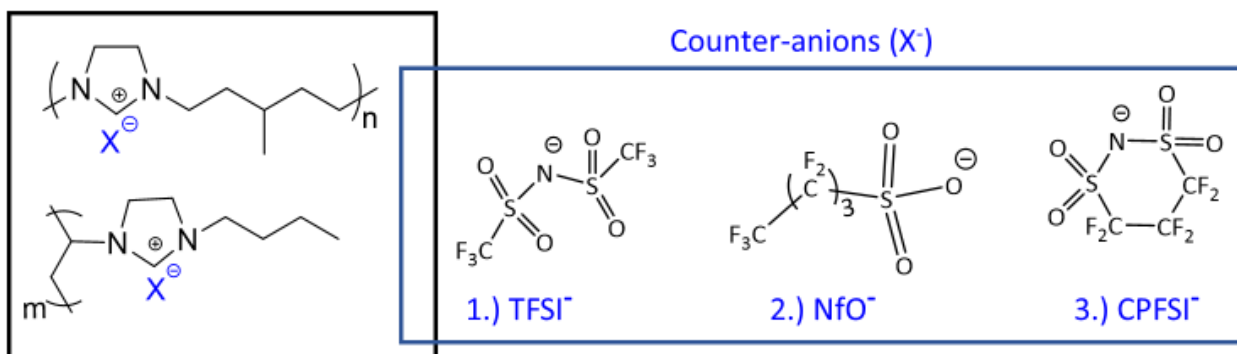
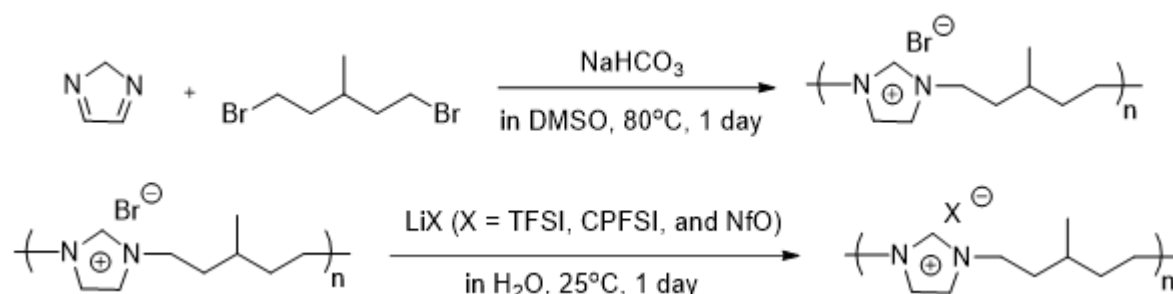


Figure 1: Chemical structures of the aliphatic imidazolium-based backbone and pendant PILs and varying counter-anions in this study.



Scheme 1. Synthesis of backbone PILs with different counter-anions via the counter-ion conversion method proposed by Marcilla et al.^{36,37} The synthesis of pendant PILs is provided in our previous work.³⁴

Figure 1 shows the chemical structures of the backbone and pendant PILs in this study. Scheme 1 summarizes the synthetic protocol for backbone PILs with different counter-anions: bis(trifluoromethanesulfonyl)imide (TFSI), 1,1,2,2,3,3-hexafluoropropane-1,2-disulfonimide (CPFSI), and nonafluorobutanesulfonate (NfO). The step-growth polymerization was

conducted by quaternizing imidazole (7.04 g) with 1,5-dibromo-3-methylpentane (25.2 g) in DMSO (34.0 mL) at 80 °C under a nitrogen atmosphere. Two molar equivalents of NaHCO₃ (8.69 g) were added to 1,5-dibromo-3-methylpentane to promote the polymerization through neutralization of the side product, hydrogen bromide. After polymerization, the obtained precipitate was dialyzed in a mixture of methanol and water (1:1 in volume percent) for 3 days using a dialysis tube (Spectra/Por 2, Spectrum Laboratories, Inc., USA) with a nominal molecular weight cutoff of 12000–14000 Da to eliminate the unreacted imidazole and 1,5-dibromo-3-methylpentane. The resultant solution was dried via freeze-drying, in which the dialyzed solution was evaporated under vacuum conditions at room temperature for 6 hours to remove the methanol. Next, approximately 10 mL of water was added into the solid sample which was then pre-frozen in a flask. The flask was then connected to a custom-made vacuum line and freeze-dried at room temperature for 15 hours. Backbone PILs with bromides as counter-anions (B-Br, 2.08 g) were obtained in powder form. Hereafter, we refer to a backbone PIL with counter-anion X as B-X.

B-PILs with different counter-anions were prepared by using the counter-ion conversion method proposed by Marcilla et al.³⁶ In one example, B-TFSI was prepared by slowly titrating an aqueous solution containing Li-TFSI (1.95 g) into an aqueous solution containing B-Br (0.467 g). The mixture was stirred for at least 1 day at 25 °C. The counter-ion conversion was immediately performed after titrating the aqueous solution of Li-TFSI, resulting in the precipitation of B-TFSI. The precipitate was washed with DI water until the filtrate remained transparent when adding an aqueous solution containing 0.1 M of AgNO₃. The molar ratio, M_r , of lithium salt to B-Br was chosen as $M_r = 3$. The purity was confirmed by elemental analysis (CHN coder MT-6, Yanako, Inc.), and the exchange rate was found to be almost 100%. Elem. Anal. Calcd for C₁₁H₁₅N₃O₄S₂F₆ (B-TFSI) (wt%): C, 30.62; H, 3.51; N, 9.74. Found (wt%): C, 30.76; H, 3.53; N, 9.67. Calcd for C₁₃H₁₅N₂O₃S₁F₉ (B-NfO) (wt%):

C, 34.67; H, 3.36; N, 6.22. Found (wt%): C, 32.72; H, 3.39; N, 6.22. Calcd for C₁₂H₁₅N₃O₄S₂F₆ (B-CPFSI) (wt%): C, 32.50; H, 3.42; N, 9.48. Found (wt%): C, 32.72; H, 3.41; N, 9.39. The preparation of pendant PILs is summarized in our previous study.³⁴ Hereafter, we refer to a pendant PIL with counter-anion X as P-X.

Characterization

I. Differential Scanning Calorimetry (DSC)

Thermal analysis was performed using a TA Instruments (New Castle, DE) Q2000 differential scanning calorimeter. Samples of 3-7 mg were placed in T-zero aluminum hermetic pans and heated at 5 °C per minute in a dry nitrogen environment (50 mL/min). The glass transition temperature was determined during the second heating cycle and evaluated as the midpoint of the heat capacity change. The melting temperature was determined from the first heating cycle as the minimum of the endothermic peak, for the purpose of maintaining similar thermal history as samples used in X-ray scattering.

II. X-ray Scattering (WAXS/SAXS)

The wide/small angle X-ray scattering experiments were performed on a laboratory beamline (Xeuss 2.0 HR, Xenocs, France) using a GeniX3D microfocus sealed tube Cu beam source with an X-ray wavelength of 1.54 Å and power settings of 50 kV and 0.6 mA. Full two-dimensional scattering patterns were collected using a Pilatus3 R200K detector, with sample to detector distances of approximately 156 mm for WAXS and 2473 mm for SAXS data collection. Samples were placed in a rubber O-ring with affixed Kapton windows to prevent leakage, and then placed in a Linkam (Tadworth, England) HFSX350 heating stage for temperature control. Samples were heated at a rate of 10 °C/minute and allowed to reach the desired temperature for 15 minutes before collecting data for 1 hour and 30 minutes. Due to crystallization in the B-PILs, the samples were heated above the melting point of the respective B-PIL (See Table I). The scattering patterns were collected using silicon scatter-less slits for

collimation (1.2 and 0.8 mm for WAXS; 0.6 and 0.5 mm for SAXS), and integrated over a tilted circle profile using Foxtrot 3.3.4 software (Xenocs, Soleil Synchrotron) to convert 2D images into one-dimensional scattering data of scattering intensity $I(q)$ (in arbitrary units) versus q (scattering vector in \AA^{-1}).

III. Densitometry

The densities, d , were determined at room temperature using a high-precision helium pycnometer (AccuPyc II 1340, Micrometrics Instrument). The detailed method was provided in our previous report.³⁸ The obtained d was 1.66 g cm^{-3} for B-CPFSI, 1.54 g cm^{-3} for B-TFSI, 1.58 g cm^{-3} for B-NfO, 1.57 g cm^{-3} for P-CPFSI, 1.52 g cm^{-3} for P-TFSI, and 1.57 g cm^{-3} for P-NfO.

IV. Dielectric Relaxation Spectroscopy (DRS)

Samples were prepared for the dielectric measurement by allowing them to flow above T_m in vacuum to cover a 20 mm diameter freshly polished brass electrode. To control the sample thickness at 0.05 mm, silica rod spacers were placed on top of the sample after it flowed to cover the electrode. Then a 10 mm diameter freshly polished brass electrode was placed on top of the sample and spacers to make a parallel plate capacitor cell which was squeezed to a gap of 0.05 mm in the Novocontrol Technologies BDS1400 preparation chamber (Montabaur, Germany), heated under vacuum of about 10^{-2} Torr. Dielectric measurements were performed using a Novocontrol Technologies Alpha High Resolution Broadband Dielectric/Impedance Spectrometer (Montabaur, Germany) with 0.1 V excitation and no bias in a dry nitrogen environment. Semi-crystalline B-PIL and amorphous P-PIL samples were heated above 100 °C (which was above T_m for all B-PIL samples) for 30 minutes until conductivity become constant from loss of water, and the spectra were obtained on cooling. The B-PILs remained amorphous during the cooling and there was no indication of crystallization.⁵ Data was

collected in isothermal frequency sweeps of 10^{-1} to 10^7 Hz from 150 °C to near T_g in steps of 5 °C using a Quatro temperature control unit.

V. DRS Analysis

The dielectric spectrum can be analyzed in terms of the complex permittivity $\epsilon^*(\omega)$, complex conductivity $\sigma^*(\omega)$, and complex electric modulus $M^*(\omega)$. These three quantities are connected by the following equations: $\epsilon^*(\omega) = \frac{\sigma^*(\omega)}{i\omega\epsilon_0} = \frac{1}{M^*(\omega)}$, where ϵ_0 is the vacuum permittivity.³⁹ Although each quantity is related, the different formalisms emphasize different aspects for the underlying dielectric processes, and thus an appropriate formalism should be selected in accordance with the appropriate purpose. Figure 2 shows representative dielectric spectra for B-TFSI at 0°C, similar to those for amorphous PILs reported in literature.^{19,23,31,32} Specifically, the dielectric relaxation process in $\epsilon''(\omega)$ is hidden by the conductivity contribution which manifests as a plateau region in $\sigma'(\omega)$, while such contribution is suppressed in $M''(\omega)$. Indeed, a peak in $M''(\omega)$ is clearly observed, and is generally attributed to the conductivity relaxation representing the start of ion diffusion since its frequency is close to the onset of $\sigma'(\omega)$ plateau (see Figure 2(b)).

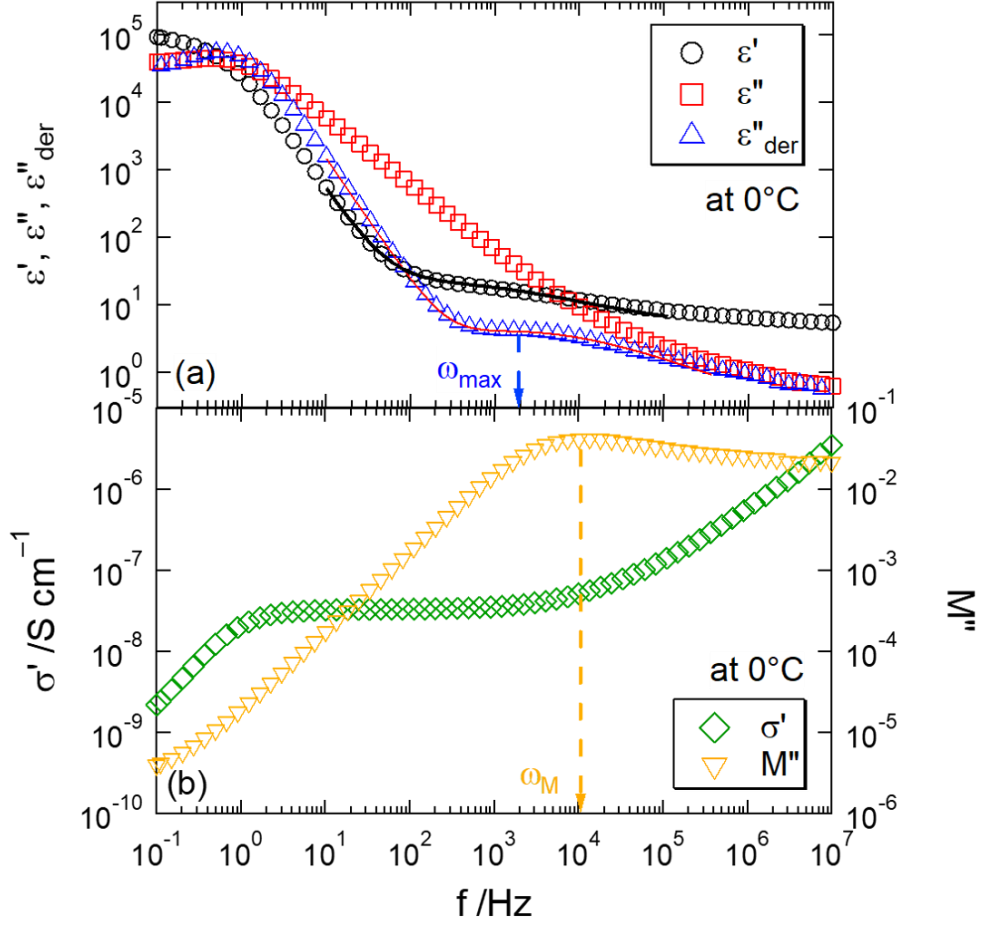


Figure 2: Dielectric response of the backbone-TFSI at 0°C in terms of (a) the complex permittivity ($\epsilon^*(\omega) = \epsilon'(\omega) - i\epsilon''(\omega)$) and the derivative loss $\epsilon''_{\text{der}}(\omega)$ and (b) the real part of conductivity $\sigma'(\omega)$, and the imaginary part of electric modulus $M''(\omega)$ as a function of frequency. The peak frequency for $\epsilon''_{\text{der}}(\omega)$, ω_{max} , and $M''(\omega)$, ω_M , is indicated by dashed arrows. The value of ω_{max} was estimated by fitting the derivative loss spectra with a derivative form of Havriliak-Negami (HN) function.

Furthermore, the measurable temperature range for ω_M is usually wider than that for ω_{max} , the frequency of maximal loss.³¹ As a result, the ion transport mechanism has been investigated through the formalisms of $\sigma^*(\omega)$ and $M^*(\omega)$ since the analyses can be performed by model-free approaches.^{17–19,31,32} On the other hand, the conductivity contribution can be eliminated by employing the derivative formalism, given by:⁴⁰

$$\varepsilon_{\text{der}} = \frac{\pi}{2} \frac{\partial \varepsilon'(\omega)}{\partial \ln \omega} \quad (1)$$

In the derivative spectra (for example, see triangles in Figure 2(a)), the B-PILs and P-PILs exhibit a relaxation process around 10^3 Hz, close to the frequency of the onset of the plateau region in $\sigma'(\omega)$ and the peak frequency in $M''(\omega)$. The conductivity relaxation time obtained from $M''(\omega)$ is generally shorter than that from $\varepsilon''_{\text{der}}(\omega)$, in agreement with our PILs.^{19,39} Moreover, we found that the temperature dependence of the peak frequency in $M''(\omega)$ was identical to that of the peak frequency in $\varepsilon''_{\text{der}}(\omega)$ (see Figure S1 of the supporting information). These results indicate that the dielectric relaxation process in $\varepsilon''_{\text{der}}(\omega)$ can be attributed to the ionic motions. We further fitted the derivative spectra with a power law fit (to account for the higher frequency contribution from electrode polarization) and a Havriliak-Negami (HN) function for the dielectric relaxation:

$$\varepsilon''_{\text{der}}(\omega) = A\omega^{-s} - \frac{\pi}{2} \left(\left[\frac{d\varepsilon'_{\text{HN}}(\omega)}{d \ln \omega} \right] \right) \quad (2)$$

$$\varepsilon'_{\text{HN}}(\omega) = \text{Real} \left\{ \frac{\Delta\varepsilon}{\left[1 + \left(\frac{i\omega}{\omega_{\text{HN}}} \right)^\alpha \right]^\beta} \right\} \quad (3)$$

in which A and s are constants, $\Delta\varepsilon$ is the relaxation strength, a and b are HN shape parameters (corresponding to high frequency skewness and breadth, respectively), and ω_{HN} is a characteristic frequency related to the frequency of maximal loss ω_{max} by:^{41,42}

$$\omega_{\text{max}} = \omega_{\text{HN}} \left(\sin \frac{a\pi}{2+2b} \right)^{1/a} \left(\sin \frac{ab\pi}{2+2b} \right)^{-1/a} \quad (4)$$

In our study, the derivative formalism was chosen to estimate the temperature dependence of $\Delta\varepsilon$ as well as that of ω_{max} ($\propto \omega_{\text{M}}$). The fitting quality was confirmed by fitting the measured real part of permittivity $\varepsilon'(\omega)$ by equation 3 with the same HN fitting parameters used for the fit of $\varepsilon''_{\text{der}}(\omega)$ (see black solid line in Figure 2(a)). Here, the electrode polarization observed in $\varepsilon'(\omega)$ at low frequencies was captured by a power law fit and the static dielectric constant at high frequency, ε_∞ , was estimated from the value of $\varepsilon'(\omega)$ at -150 °C.

VI. Rheology

The complex shear modulus $G^*(\omega) = G'(\omega) + iG''(\omega)$, with $G'(\omega)$ and $G''(\omega)$ being storage and loss moduli, at frequencies ranging from 0.1 to 100 rad s⁻¹ was measured by using a strain controlled rheometer (ARES-G2, TA Instruments) with a custom fabricated parallel disk geometry having a 4 mm diameter. The strain amplitude varied between 0.01 and 20% to acquire torques much higher than the minimum measurable torque in oscillation for the ARES-G2 ($T_{\min,osc} = 0.05 \mu\text{N m}$ as specified by the manufacturer). The linear regime was confirmed by strain sweep measurements in which the values of $G^*(\omega)$ were independent of strain. The $G^*(\omega)$ dependence on frequency was obtained in a temperature range from -26 to 100 °C under a nitrogen atmosphere. Prior to being loaded between the parallel plates, polymer samples in powder form were melted into 4 mm diameter disks with a thickness of about 1.5 mm. To estimate $G^*(\omega)$ for B-PILs in the amorphous state, the measurements at temperatures lower than T_m were performed immediately after quenching the loaded sample from a temperature higher than T_m . This procedure enables us to construct the composite curve of $G^*(\omega)$ over more than 10 decades of frequency, resulting in an estimate of the dependence of the characteristic chain relaxation time as a function of temperature.

3. Results/Discussion

Morphology

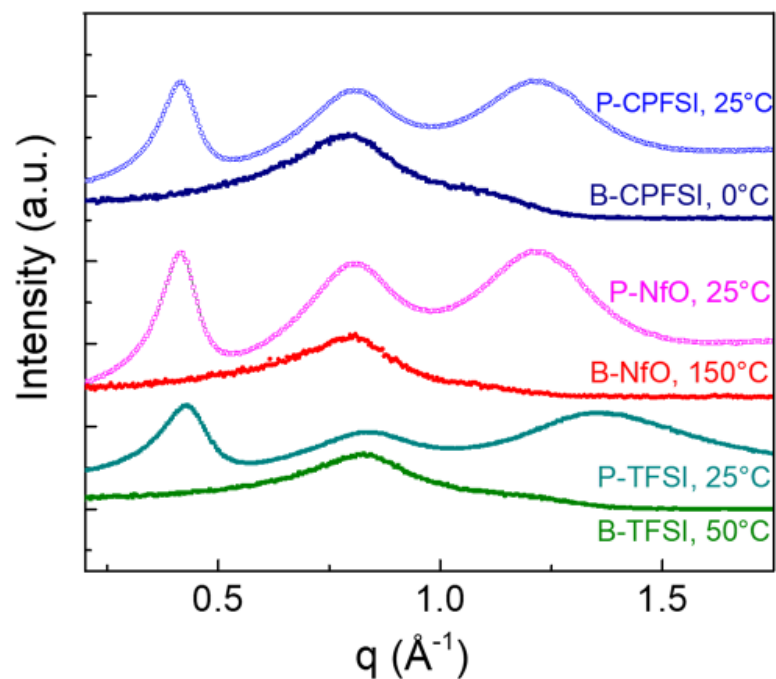


Figure 3: Comparison of wide-angle X-ray scattering data between pendant and backbone PILs. X-ray scattering were acquired for the respective B-PIL at or above the T_m to account for differences in scattering due to the crystalline nature of the as-prepared B-PILs at room temperature. The scattering data was vertically shifted for clarity.

Table I. Correlation distances (from WAXS) and glass transition temperatures (from DSC) of B-PILs and P-PILs.

	Backbone-backbone (Å)	Anion-anion (Å)	Pendant-pendant (Å)	T _g (°C)	T _m (°C)
P-CPFSI	15	7.9	5.2	100	-
B-CPFSI	-	7.9	-	8	100
P-NfO	15	7.8	5.0	128	-
B-NfO	-	7.8	-	28	125
P-TFSI	15	7.6	4.8	50	-
B-TFSI	-	7.6	-	-30	42

Figure 3 compares the WAXS profiles for P-PILs and B-PILs with TFSI, CPFSI, and NfO counter-anions. Due to crystallinity in the B-PIL samples, WAXS patterns for B-PILs were recorded at temperatures above the respective B-PIL T_m to observe only the amorphous and ionic scattering (see Figure S2 for WAXS patterns of the semi-crystalline B-PILs). For P-PILs, WAXS patterns were recorded at room temperature since the overall shape of the WAXS patterns is independent of temperature, even at temperatures well above T_g (see Figure S3 of the supporting information).¹⁶ In the pendant PIL scattering profiles, three peaks can be observed: the pendant-pendant correlation peak (q_p), the anion-anion correlation peak (q_a), and the backbone-backbone correlation peak (q_b). In the backbone PIL scattering profiles, a significant peak at 0.8 Å⁻¹ was observed that was independent of the type of counter-anion. The corresponding correlation length (7.8 Å) was comparable to the distance between imidazolium rings connected by pentyl groups with an extended zigzag conformation (7.2 Å). Since there are likely differences in electron density between ionic groups and alkyl groups, this result indicates that the scattering peak at 0.8 Å⁻¹ is assigned to the ion-ion correlation peak. At 1.1 Å⁻¹, a consistent shoulder was observed, likely due to the amorphous halo from the 3-

methylpentane group.⁴³ Bragg's law relates scattering lengths with correlation distances by the relation $d_x = 2\pi/q_x$, which are reported in Table I and agree with prior simulation/experimental work.^{16,22,23,34,44,45} Due to the absence of pendant groups in the B-PILs, there were no observed pendant-pendant and backbone-backbone correlation peaks at $T > T_m$.

Scattering profiles also show that anion-anion correlation peaks do not change in equivalent pendant and backbone PILs with the same counter-anion at the same temperature. This observation may be attributed to the anion-anion correlation distance in the studied B-PILs (approximately equivalent to the distance between subsequent imidazolium groups on the backbone chain) to be equivalent to the distance between imidazolium groups on subsequent side chains in P-PILs.

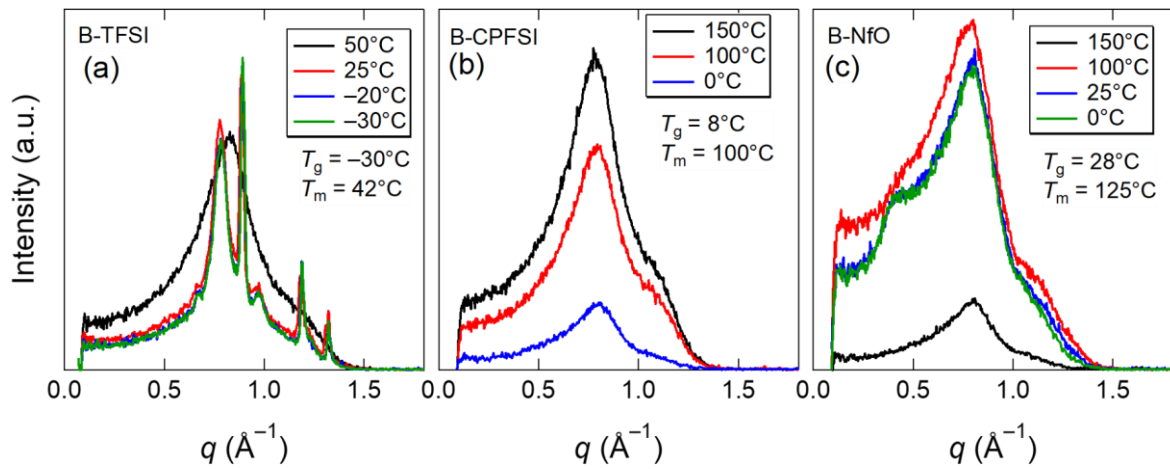


Figure 4: An additional X-ray scattering peak is emerged at 0.4 \AA^{-1} for B-NfO as temperature decreases. In the plot, the wide-angle X-ray scattering pattern for (a) B-TFSI, (b) B-CPFSI, and (c) B-NfO at different temperatures spanning T_g and T_m are reported. The change in the WAXS pattern is monitored while cooling down from a temperature above T_m .

Figure 4 shows the temperature dependence of WAXS pattern for B-PILs in a temperature range spanning T_g and T_m . The crystallization took place at temperatures between

T_m and T_g (see Figure 4(a)). Nevertheless, no additional peaks were observed for B-TFSI (Figure 4(a)) and B-CPFSI (Figure 4(b)). On the other hand, we found that for B-NfO, an additional peak at 0.4 \AA^{-1} became more pronounced as temperature decreases and then its intensity became constant at temperatures below T_g , indicating a morphological change of B-NfO. Comparing the chemical structure of counter-anions, we hypothesize that NfO anions form nanosegregated fluorine domains owing to their relatively long fluoroalkyl segments. Indeed, Pereiro et al.^{46,47} reported that fluoroalkyl segments can act as apolar groups in ionic liquids and form fluorinated aggregates showing a scattering peak around 0.4 \AA^{-1} .⁴⁷ Since the nanosegregated fluorine domains are composed of mobile NfO counter-anions, they may be disrupted at elevated temperatures.

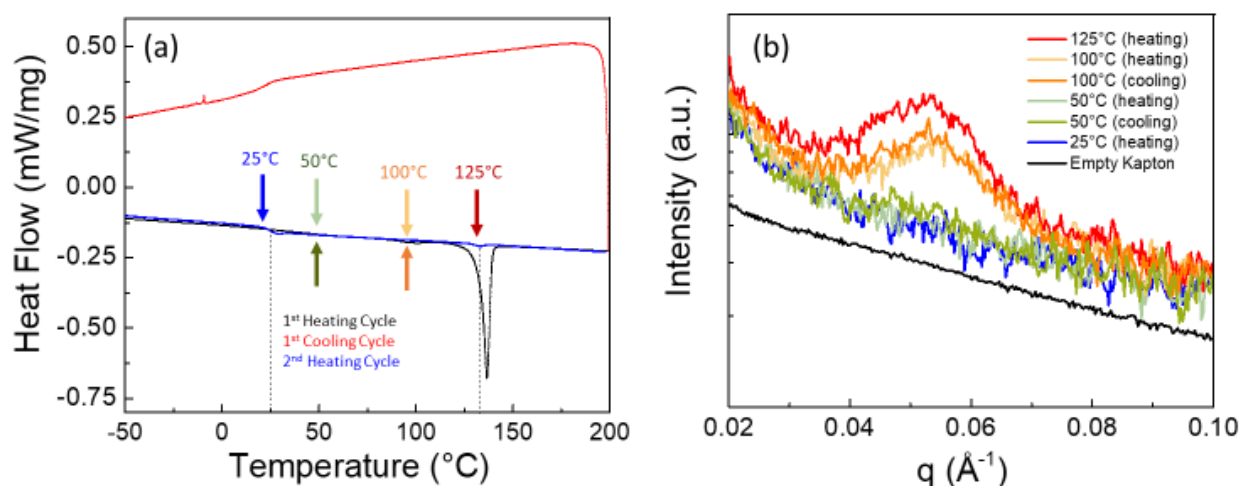


Figure 5: (a) Differential scanning calorimetry heating profile of B-NfO shows a T_g of 28 °C and T_m of 125 °C. (b) Small-Angle X-ray scattering data of B-PIL NfO shows a thermally reversible ionic aggregation peak.

To further investigate the observed morphological change of B-NfO, we performed small angle X-ray scattering measurements while varying temperature at scattering angles ranging from 0.02 to 0.1 \AA^{-1} . Figure 5 exhibits the thermal analysis obtained from DSC (left) and the scattering profile of B-NfO (right), showing a thermally reversible correlation peak at

0.053 Å⁻¹ ($d = 11.8$ nm). In contrast to the WAXS profiles in Figure 4(c), the SAXS peak at 0.053 Å⁻¹ became more pronounced as temperature increased. Such a peak was not observed for B-TFSI, P-NfO, and B-CPFSI as shown in Figures S4–S6 of the supporting information. A similar SAXS peak was observed in a crystalline backbone PIL with a TFSI counter-anion.⁵ However, the crystallization of the B-NfO sample did not occur in the experimental time scale, resulting from the absence of clear sharp peaks in the WAXS profiles shown in Figure 4(c). Alternatively, we speculate that B-NfO forms fewer and weaker ionic aggregates with increasing temperature, since a similar small ionomer peak, assigned to the ion aggregation, is observed at 0.06 Å⁻¹ for ionomers with ionic liquid-based counter-ions.⁴⁸ We propose that the different chemical features of NfO anions, such as the long fluoralkyl segments and the location of negative charges, play a key role in determining the morphology of B-NfO. However, further investigation is needed to understand why only B-NfO forms ionic aggregates and why its morphology depends on temperature.

Rheological Measurements

I. Complex Modulus

Figure 6 displays the composite curve of the complex shear modulus $G^*(\omega) = G'(\omega) + iG''(\omega)$ for B-PILs. The obtained spectra at various temperatures were reduced at a reference temperature by using the method of reduced valuables: the angular frequencies are reduced with the viscoelastic shift factors a_T . The reference temperature was chosen as the temperature at which the peak frequency of $G''(\omega)$ in the glassy zone is located at approximately 10^7 rad s⁻¹ and was approximately $T_g + 50$ °C for each B-PIL sample. The method of reduced valuables, i.e. the time-temperature superposition principle (TTS), worked well, in the measured temperature range for B-TFSI. However, TTS for B-NfO and B-CPFSI did not hold

in an intermediate temperature range where either crystallization or a morphological change (only for B-NfO) takes place. Therefore, the composite curve of $G^*(\omega)$ at $\omega a_T < 10^2 \text{ rad s}^{-1}$ was constructed such that an extrapolated line of $G''(\omega)$ towards high frequencies overlaps with $G''(\omega)$ at $\omega a_T > 10^2 \text{ rad s}^{-1}$.

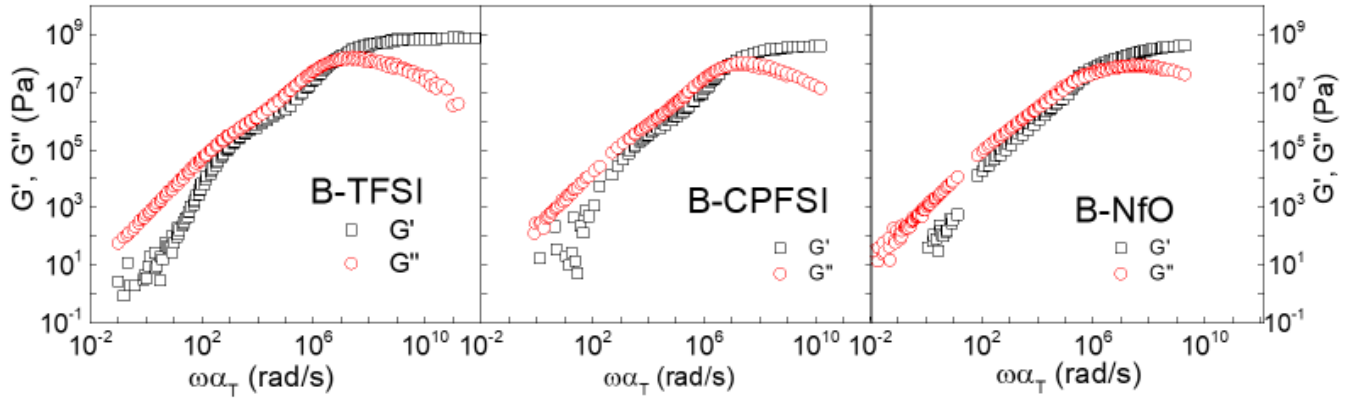


Figure 6. Complex modulus $G^*(\omega)$ dependence on frequency for the B-PILs depends on the type of counter-anions. The complex shear modulus $G^*(\omega) = G'(\omega) + iG''(\omega)$ for (a) B-TFSI, (b) B-CPFSI, and (c) B-NfO is plotted as a function of reduced frequency. The reference temperature is chosen as the temperature at which the peak frequency of $G''(\omega)$ in the glassy zone is located around 10^7 rad s^{-1} . The missing points in Figures 6(b) and (c) are mainly due to the crystallization of B-CPFSI and B-NfO occurred during measurement. Rheological measurements in the amorphous state were performed by repeatedly heating the sample above T_m and subsequent quenching at the target temperature. The temperature range measured was from 15 to 130 °C. Black squares: storage modulus, Red circles: loss modulus.

We observed typical linear viscoelastic responses for amorphous polymers. When $10^{-1} \text{ rad s}^{-1} < \omega a_T < 10^5 \text{ rad s}^{-1}$, the power law relationships of $G'(\omega)$ and $G''(\omega)$ with respect to frequency, i.e. $G'(\omega), G''(\omega) \propto \omega^n$, were observed, while varying the power index (n) from $n = 2$ to $n = 1/2$ for $G'(\omega)$ and from $n = 1$ to $n = 1/2$ for $G''(\omega)$. The observed

power law indexes are identical with those observed for ordinary amorphous polymers in rubbery and terminal zones. The rubbery plateau regime was not observed due to the insubstantial number of entanglements in the B-TFSI sample. The molecular weight $M = 2.0 \times 10^4 \text{ g mol}^{-1}$ of B-TFSI was estimated by fitting the rubbery and terminal zones with the Rouse model (see Figure S7). At frequencies ranging from 10^5 to $10^{11} \text{ rad s}^{-1}$, the values of $G'(\omega)$ increased with $n = 1$ until $\omega = 10^7 \text{ rad s}^{-1}$ and then approached to $G'(\omega) = 10^9 \text{ Pa}$, while the values of $G''(\omega)$ increased with $n = 1$ and then started to decrease with increasing ω around $\omega = 10^7 \text{ rad s}^{-1}$. This frequency regime can be potentially assigned to the glass-to-rubber transition and glassy zones. Similar dependence of $G^*(\omega)$ over the measured frequency range was observed for B-CPFSI. On the other hand, for B-NfO, the $G^*(\omega)$ dependence on frequency ranging from 10^{-1} to 10^3 rad s^{-1} , i.e. the terminal zone, was similar to that for B-TFSI, while the $G^*(\omega)$ dependence on frequency in the glass-to-rubber and glassy zones for B-NfO, i.e., $10^3 \text{ rad s}^{-1} < \omega a_T < 10^{11} \text{ rad s}^{-1}$, was different from that for B-TFSI. The values of $G'(\omega)$ increased more steeply ($n=0.85$) with increasing ω and the dependence of $G''(\omega)$ on frequency became broader compared to those for B-TFSI. Similar broadening of linear viscoelastic spectra in the glass-to-rubber transition zone is observed in P-PILs.⁴⁴ Nevertheless, the longest relaxation time, calculated from the intersection of the two slopes of $G'(\omega)$ and $G''(\omega)$ in the terminal zone, was 1.2 ms for B-CPFSI, 1.9 ms for B-NfO, and 2.2 ms for B-TFSI at the reference temperature. Thus, the molecular weights for the B-PILs investigated are similar to one another

I. Chain Relaxation

To characterize the polymer dynamics of B-PILs and P-PILs, the crossover frequency ω_α of $G'(\omega)$ and $G''(\omega)$ in the glassy zone at each temperature was estimated by:

$$\omega_\alpha(T) = \omega_\alpha(T_r) a_T(T) \quad (5)$$

where T_r is the reference temperature. Figure 7 shows the dependence of ω_α versus inverse temperature plot for the B-PILs and the P-PILs. The crossover frequency ω_α was found to follow a Vogel-Fulcher-Tammann (VFT) type of temperature dependence over the measured temperature range:

$$\omega_\alpha(T) = \omega_\infty \exp\left(-\frac{DT_0}{T-T_0}\right) \quad (6)$$

where ω_∞ is the high-temperature limit of the peak frequency, T_0 is the Vogel temperature, and D is the so-called strength parameter. The estimated values are summarized in Table II. The values of VFT parameters depended on both the type of counter-anions and the charge placement.

To further understand this trend, we calculated the fragility m for each PIL by using the following equation:⁴⁹

$$m = \frac{DT_0T_g}{(T_g-T_0)^2(\ln(10))} \quad (7)$$

The estimated values are summarized in Table II. The trend of m versus T_g for PILs was opposite to that for non-ionic amorphous polymers for which, in general, lower T_g is correlated to lower fragility.⁴⁹ The presence of the rigid imidazole ring on the side chains is expected to increase both m and T_g according to Kunal et al.⁴⁹ However, B-CPFSI and B-TFSI display a higher m value and lower T_g , compared to their P-PIL counter-parts. This can be explained by the movement of relatively large counter-anions below T_g observed only for the P-PIL samples. On the other hand, the PILs with NfO anions show relatively smaller m , although their T_g is the highest among the PILs studied. Comparing the chemical structure of NfO anions, we hypothesize that the relatively flexible fluoroalkyl segments and the difference in the ion-ion interaction between NfO anions and imidazolium cations in NfO anions influence

the trend of m versus T_g . However, further investigation is required to comprehensively understand the relationship between m , T_g , and the chemical structure of PILs.

Table II. VFT parameters, D , and T_0 for ω_α fragility, m , and glass transition temperature, T_g of P-PILs and B-PILs.

Polymer Sample	D	T_0 (K)	m	T_g (°C)
B-TFSI	5.5	215	151	−30
P-TFSI	9.7	250	63	50
B-CPFSI	2.8	256	136	8
P-CPFSI	9.6	285	56	100
B-NfO	5.3	247	58	28
P-NfO	8.2	321	71	128

Dielectric Response

I. Dielectric Relaxation and Comparison to Rheology

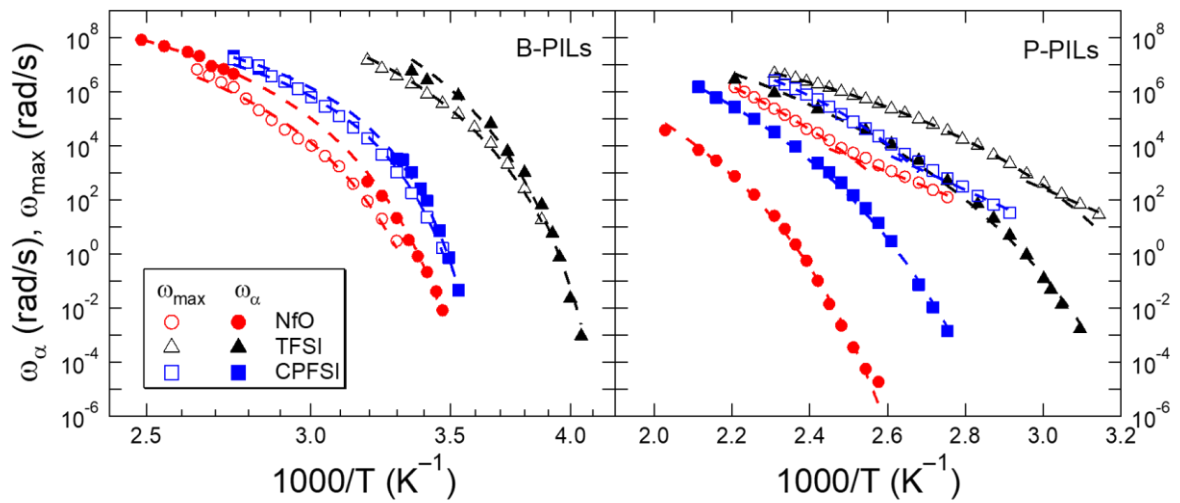


Figure 7. Temperature dependence of peak frequency from rheological measurements (ω_α) and from dielectric measurements (ω_{\max}). ω_α in the glassy zone displays a VFT type of temperature dependence over the measured temperature range for B-PILs and P-PILs. Dashed lines indicate the best VFT fits with fitting parameters provided in Table II. The missing points of ω_α for B-CPFSI and B-NfO may be mainly due to the crystallization of the sample during rheological measurements. ω_{\max} exhibits a VFT type of temperature dependence for B-PILs, but a VFT to Arrhenius type transition for P-PILs below the glass transition temperature. Dashed lines indicate the best VFT and Arrhenius fits with fitting parameters provided in Table III.

Table III: VFT parameters D , and T_0 and activation energy E_a , ω_{\max} for P-PILs and B-PILs.

	D	T_0 (K)	E_a (kJ/mol)
B-TFSI	5.6	212	-
P-TFSI	6.1	248	118
B-CPFSI	3.0	255	-
P-CPFSI	4.2	300	125
B-NfO	5.3	250	-
P-NfO	10.8	263	108

A characteristic feature for the ion transport mechanism of PILs is that the ion conduction can be decoupled from the segmental motions of polymer chains near T_g .^{9,30} Figure 7 compares the temperature dependence of the peak frequency ω_{\max} for the ionic motions with

that for segmental motions ω_a . For P-PILs, the values of ω_{\max} were captured by either VFT or Arrhenius equations:

$$\omega_{\max} = \omega_{\infty} \exp\left(-\frac{E_a}{RT}\right) \text{ for } T < T_g \quad (8)$$

$$\omega_{\max} = \omega_{\infty} \exp\left(-\frac{DT_0}{T-T_0}\right) \text{ for } T > T_g \quad (9)$$

The dotted lines in Figure 7 are fits to equation 8 using the strength parameter (D) and Vogel temperature (T_0) as fitting parameters, and to equation 9 using the activation energy (E_a) as a fitting parameter. The estimated values are summarized in Table III. The transition from VFT to Arrhenius behavior was observed in the vicinity of T_g , in good agreement with the literature reports for P-PILs.³⁴ This result indicates the decoupling of the ion transport from the segmental dynamics since they showed a VFT type temperature dependence even below T_g . Stacy et al.³⁵ reported that the ionic conductivity below T_g for PILs with larger counterions is controlled by elastic forces, and exhibits an activation energy of the order of 100 kJ/mol, in good agreement with the value of E_a obtained in our study. On the other hand, the values of ω_{\max} for B-PILs displayed a VFT type temperature dependence over the measured temperature range. Moreover, the agreement of VFT parameters from both the rheological and dielectric experimental data suggests that the ion motions for B-PILs are coupled to the segmental motions of polymers, which is further confirmed by a Walden plot discussed below. It should be also noted that the temperature dependence of ω_{\max} for B-NfO is appeared to be captured by a single VFT equation across the temperature range where the morphological change is observed in the scattering data. This result suggests that the morphological change shows little effect on the ionic motions probably due to the fewer and weaker ionic aggregates.

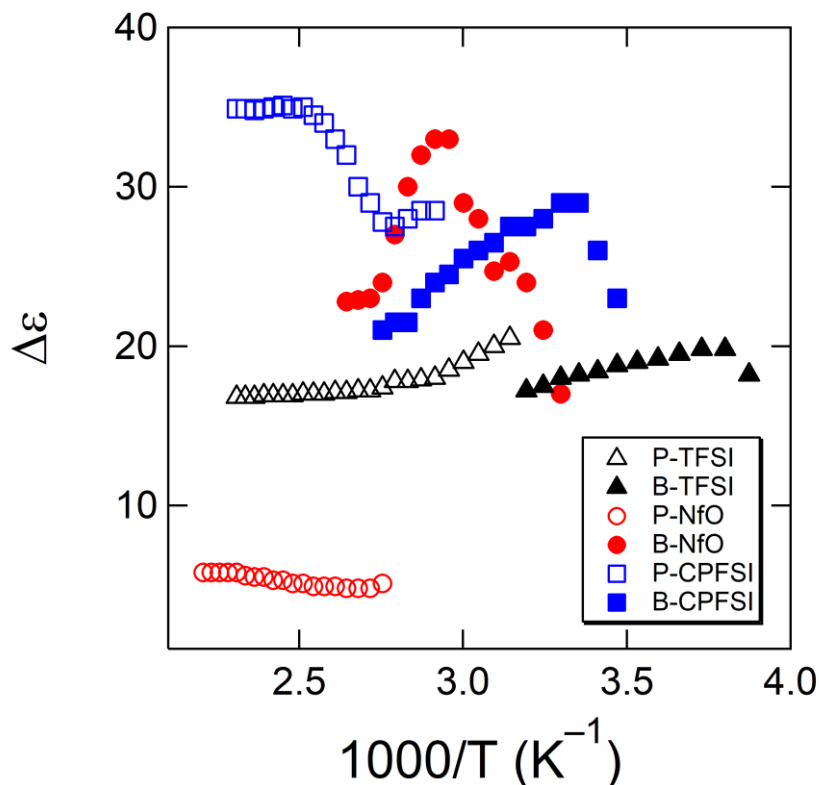


Figure 8: Temperature dependence of the dielectric relaxation strength $\Delta\epsilon$ for B-PILs (filled) and P-PILs (open) with TFSI (black), NfO (red), and CPFSI (blue) counter-anions. The value of $\Delta\epsilon$ is estimated from the fit of ϵ''_{der} with equations 2 and 3.

On the other hand, the dielectric relaxation strength $\Delta\epsilon$ exhibited evidence of the formation of ionic aggregates in B-NfO. Figure 8 shows the temperature dependence of the dielectric relaxation strength obtained from the fit of the derivative loss with equation 2. Regardless of the type of PILs, the value of $\Delta\epsilon$ followed the Onsager equation⁵⁰ at temperatures well above T_g , indicating that the dielectric relaxation strength decreases with increasing temperature arising from thermal dipole randomization. In the vicinity of T_g , $\Delta\epsilon$ decreased with decreasing temperature, resulting from the restriction of rotation/alignment of dipoles by neighboring dipoles. Similar behavior in $\Delta\epsilon$ (or static dielectric constant) has been observed in ionomers including PILs.^{20,25,51} For B-NfO, a sharp drop of $\Delta\epsilon$ was observed in a temperature range of $70\text{ }^\circ\text{C} < T < 95\text{ }^\circ\text{C}$, similar to the temperature range where the morphological change

is observed in the scattering data. When ionic aggregates are formed, the value of $\Delta\epsilon$ is usually considered to decrease because of the offset of the dipole moment of one ion pair by surrounding ion pairs. Therefore, such reduction in $\Delta\epsilon$ for B-NfO suggests the formation of ionic aggregates as temperature increases.

Comparing $\Delta\epsilon$ between B-PILs and P-PILs, the magnitude of $\Delta\epsilon$ for B-TFSI was similar to that for P-TFSI, while $\Delta\epsilon$ for P-CPFSI was larger than that for B-CPFSI. On the other hand, the values of $\Delta\epsilon$ for P-NfO was much smaller than that for B-NfO. For ionomer systems, the magnitude of $\Delta\epsilon$ can be proportional to the product of the number density of ion pairs and the square of dipole moment of those ion pairs.²⁶ Furthermore, for PILs with the same ion pairs, the value of $\Delta\epsilon$ could be simply determined by the number density of ion pairs. Bearing this in mind, the larger $\Delta\epsilon$ for P-CPFSI suggests that the number of conducting CPFSI anions in P-CPFSI is larger than that in B-CPFSI. In contrast, the number of conducting NfO anions in P-NfO is much smaller than that in B-NfO.

Ionic Conductivity

Figure 9 shows the ionic conductivity data for the B-PILs and P-PILs measured using DRS both as a function of temperature and scaled to T_g , to elaborate differences between the respective temperature scales. The charge densities of the B-PILs are similar to that of the P-PILs, given the similarity in chemical structure of the repeat units of the two polymers. B-PILs exhibited higher conductivity on an absolute temperature scale, which is attributed to the lower glass transition temperatures, compared to equivalent P-PILs.

Fan et al.³¹ has reported that the dynamics of PILs become independent of molecular weight once the molecular weight exceeds a certain critical molecular weight at which the segmental motion is observed in mechanical responses, i.e., polymeric behavior. Since the molecular weights of the B-PILs and P-PILs are near or exceed that critical molecular weight,

we can conclude that the molecular weights of these materials do not affect the observed conductivity (Figure 6 and S8). The lower T_g of B-PILs and corresponding higher conductivity compared to the equivalent P-PILs is attributed to the higher flexibility of B-PILs, which is consistent with prior experimental studies.^{5,20,52} Evans et al.⁵ found that the B-PIL with counter-ion TFSI (T_g : -35 °C) exhibited higher conductivity than the equivalent P-PIL (T_g : 16 °C) when temperature is normalized by T_g . This difference was attributed to the more percolated pathway for the TFSI counter-anion in the B-PIL sample and was most apparent at the glass transition temperature of each respective material. However, as shown in Figure 9(b), T_g -normalized conductivity for our B-PILs exhibited lower conductivity than that for P-PILs regardless of the type of counter-anions. We speculate that acrylamide groups on the side chains of P-PILs of Evans et al. form hydrogen bonding to counter-anions, leading to lower T_g -normalized ionic conductivity. Moreover, it seems that the T_g -normalized conductivity for our P-PILs overlaps with that for our B-PILs when extrapolating toward high temperatures. These results suggest that the underlying ion transport mechanism for B-PILs and P-PILs is the same with different degree of decoupling of the ion transport from the segmental dynamics.

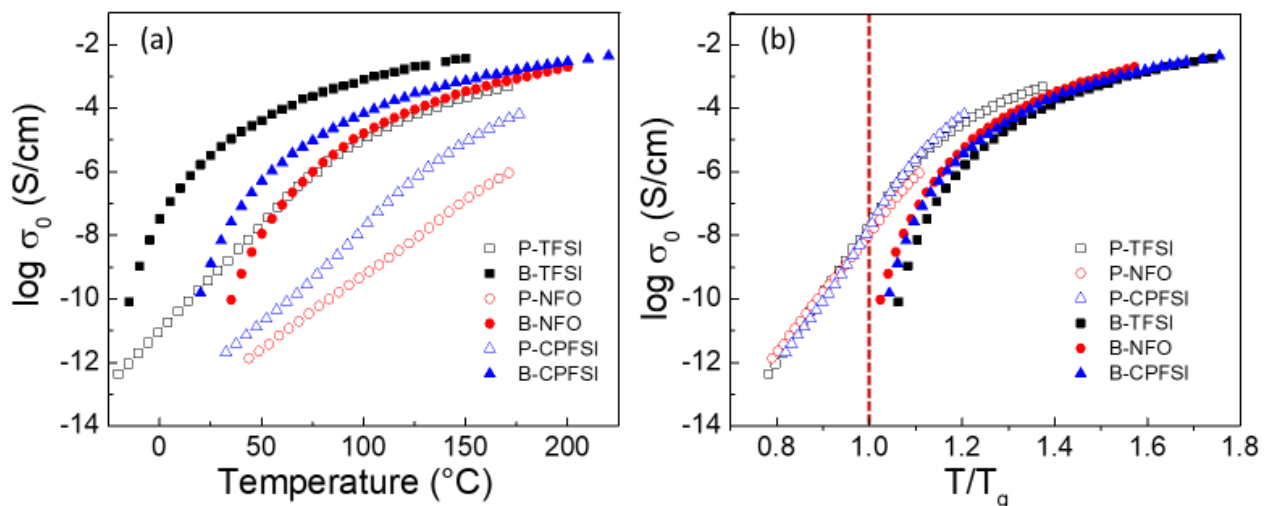


Figure 9: (a) The conductivity profiles of B-PILs and P-PILs from DRS is shown as a function of temperature, and (b) scaled to each material's respective glass transition temperature (right).

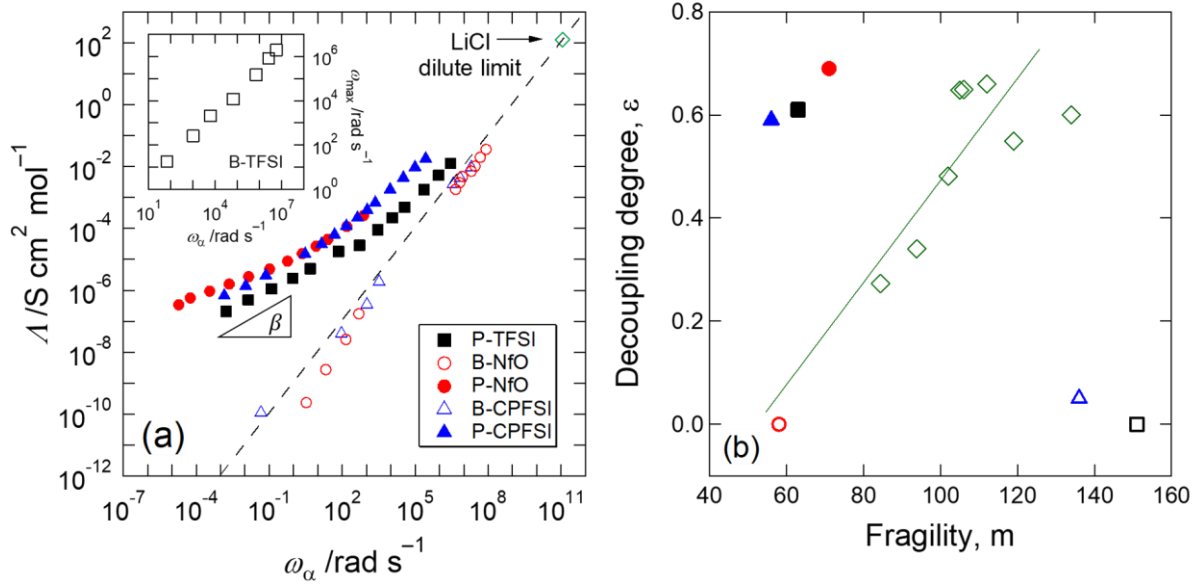


Figure 10: (a) Relationship of the molar conductivity Λ to the structural relaxation rate ω_α for P-PILs (filled) and B-PILs (open) with TFSI (black squares), NfO (red circles), and CPFSI (blue triangles). Because of the lack of data for B-TFSI, the insert shows the dielectric relaxation rate ω_{\max} as a function of ω_α . The value of Λ and ω_α for LiCl in dilute limit is taken from ref.31 (b) Degree of decoupling, ε is plotted as a function of fragility m . Green diamonds represent data from ref.31 for the ammonium-based PILs with various side-chain lengths and molecular weights. The green line is a guide for the eyes taken from ref.31

Sokolov and coworkers proposed that the degree of decoupling shows a good correlation with the fragility m . According to their work, the degree of decoupling ε can be estimated by plotting the molar conductivity $\Lambda(= \frac{\sigma_0 M_0}{d})$ as a function of ω_α , the so-called modified Walden plot. Here, M_0 is the molar mass of one repeating unit associated with one counter-anion. For B-TFSI, the measured temperature range for σ_0 did not overlap with that for ω_α , and therefore we estimated the value of ε from the plot of ω_{\max} versus ω_α (see the insert of Figure 10(a)). Figure 10(a) shows the modified Walden plot for P-PILs (filled symbols) and B-PILs (open symbols), indicating that P-PILs showed the decoupling behavior of the ion

transport from the segmental dynamics at low ω_α , i.e., below T_g , while the ion transport for B-PILs was coupled to the segmental motions. The degree of decoupling ϵ was then estimated from a power law regime, i.e., $\Lambda \propto \omega_\alpha^{1-\epsilon}$, observed at low ω_α . Figure 10(b) compares the value of ϵ with that from previous reports.³¹ For B-PILs, no correlation between ϵ and m was observed. On the other hand, we found that imidazolium-based PILs exhibited a stronger decoupling than other ion-conducting polymers although the trend of ϵ versus m was similar. This result indicates that another factor, e.g., the correlation distance between backbones,^{16,22} plays a role in the decoupling degree in addition to the fragility of polymers.

4. Conclusions

This work explores the morphological, conductive, and rheological differences between imidazolium-based backbone and pendant PILs. Wide-angle X-ray scattering confirmed the morphology of the PILs and showed similar anion-anion correlation differences between equivalent B-PILs and P-PILs with the same counter-anions. However, dielectric relaxation spectroscopy revealed that B-PILs exhibited a higher ionic conductivity on an absolute temperature scale, while P-PILs showed both higher conductivity when scaled to the glass transition temperatures and conductivity below the glass transition temperature, attributed to the movement of the counter-anions among the side chains in P-PILs (difference in the degree of decoupling). Moreover, we found that the ion transport for B-PILs is coupled to the segmental motions of polymer chains, while that for P-PILs is decoupled from the segmental dynamics near T_g .

Associated Content

WAXS diffraction pattern for P-CPFSI at 25 °C and 0°C, WAXS diffraction patterns for B-PILs at 25 °C, DSC thermograms and SAXS diffraction patterns for B-TFSI, P-NfO, B-CPFSI, complex modulus for B-TFSI, P-TFSI, P-CPFSI, and P-NfO, Modulus'' and derivative of

permittivity function for B-TFSI and P-TFSI, and static dielectric constant as a function of frequency at varying temperatures for B-CPFSI and P-CPFSI.

Supporting Information is available free of charge on the ACS Publications website at DOI:

Acknowledgments

The authors thank Nichole Wonderling and Natalie Mamrol for assisting in X-ray scattering experiments in the Penn State Materials Research Institute Materials Characterization Lab and Renxuan Xie and Albree Weisen for assisting in sample preparation. This work was supported by the National Science Foundation and Japanese Society for the Promotion of Science East Asian Pacific Summer Institute Fellowship (Award #: 1713929) and by (DMR- 1505953 to JPR). The authors of this work also gratefully acknowledge the support of the Okinawa Institute of Science and Technology Graduate University with subsidy funding from the Cabinet Office, Government of Japan.

References

1. MacFarlane, D.R.; Forsyth, M.; Howlett, P.C.; Kar, M.; Passerini, S.; Pringle, J.M.; Ohno, H.; Watanabe, M.; Yan, F.; Zheng, W.; Zhang, S.; Zhang, J. Ionic liquids and their solid-state analogues as materials for energy generation and storage. *Nature Reviews Materials*, **2016**, 1, 15005
2. Weingärtner, H. Understanding Ionic Liquids at the Molecular Level: Facts, Problems, and Controversies. *Angew. Chem. Int. Ed.* **2008**, 47, 654-670.
3. Valderrama, J. O.; Rojas, R. E. Critical Properties of Ionic Liquids. Revisited. *Ind. Eng. Chem. Res.* **2009**, 48, 6890-6900.
4. Yuan, J.; Mecerreyes, D.; Antonietti, M. Poly(ionic liquid)s: An update. *Progress in Polymer Science* **2013**, 38, 1009-1036.

5. Evans, C. M.; Bridges, C.R.; Sanoja, G.E.; Bartels, J.; Segalman, R.A. Role of Tethered Ion Placement on Polymerized Ionic Liquid Structure and Conductivity: Pendant versus Backbone Charge Placement. *ACS Macro Lett.* **2016**, 5, 925-930.
6. Makrocka-Rydzik, M.; Glowinkowski, S; Jurga, S; Meyer, W.H. Molecular dynamics in stiff ionene below glass transition. *Solid State Nuclear Magnetic Resonance* **1995**, 4, 353-360.
7. Angell, C.A. Recent developments in fast ion transport in glassy and amorphous materials. *Solid State Ionics* **1986**, 18, 72-88.
8. Ratner, M.A.; Shriver, D.F. Ion Transport in Solvent-Free Polymers. *Chem. Rev.* **1988**, 88, 109-124.
9. Sangoro, J.R.; Iacob, C; Agapov, A.L.; Wang, Y.; Berdzinski, S.; Rexhausen, H.; Strehmel, V.; Friedrich, C.; Sokolov, A.P.; Kremer, F. Decoupling of ionic conductivity from structural dynamics in polymerized ionic liquids. *Soft Matter* **2014**, 10, 3536-3540.
10. Hall, L. M.; Stevens, M. J.; Frischknecht, A. L. Effect of Polymer Architecture and Ionic Aggregation on the Scattering Peak in Model Ionomers. *Phys. Rev. Lett.* **2011**, 106, 127801.
11. Imrie, C.T.; Ingram, M.D.; McHattie, G.S.; Ion Transport in Glassy Polymer Electrolytes. *J. Phys. Chem. B* **1999**, 103, 4132-4138.
12. Pipertzis, A.; Mühlinghaus, M.; Mezger, M.; Scherf, U.; Floudas, G. Polymerized Ionic Liquids with Polythiophene Backbones: Self-Assembly, Thermal Properties, and Ion Conduction. *Macromolecules* **2018**, 51, 6440–6450.
13. Erwin, A. J.; Lee, H.; Ge, S.; Zhao, S.; Korolovych, V. F.; He, H.; Matyjaszewski, K.; Sokolov, A. P.; Tsukruk, V. V. Viscoelastic properties and ion dynamics in star-shaped polymerized ionic liquids. *European Polymer Journal* **2018**, 109, 326–335.

14. Chen, M.; Dugger, J. W.; Li, X.; Wang, Y.; Kumar, R.; Meek, K. M.; Uhrig, D. W.; Browning, J. F.; Madsen, L. A.; Long, T. E.; Lokitz, B. S. Polymerized Ionic Liquids: Effects of Counter-Anions on Ion Conduction and Polymerization Kinetics. *Journal of Polymer Science, Part A: Polymer Chemistry* **2018**, 56, 1346–1357.
15. Frenzel, F.; Guterman, R.; Anton, A. M.; Yuan, J.; Kremer, F. Molecular Dynamics and Charge Transport in Highly Conductive Polymeric Ionic Liquids. *Macromolecules* **2017**, 50, 4022–4029.
16. Delhorbe, V.; Bresser, D.; Mendil-Jakani, H.; Rannou, P.; Bernard, L.; Gutel, T.; Lyonnard, S.; Picard, L. Unveiling the Ion Conduction Mechanism in Imidazolium-Based Poly(ionic liquids): A Comprehensive Investigation of the Structure-to-Transport Interplay. *Macromolecules* **2017**, 50, 4309–4321.
17. Wojnarowska, Z.; Feng, H.; Diaz, M.; Ortiz, A.; Ortiz, I.; Knapik-Kowalczyk, J.; Vilas, M.; Verdía, P.; Tojo, E.; Saito, T.; Stay, E. W.; Kang, N.; Mays, J. W.; Kruk, D.; Włodarczyk, P.; Sokolov, A. P.; Bocharova, V.; Paluch, M. Revealing the Charge Transport Mechanism in Polymerized Ionic Liquids: Insight from High Pressure Conductivity Studies. *Chem. Mater.* **2017**, 29, 8082–8092.
18. Wojnarowska, Z.; Knapik, J.; Jacquemin, J.; Berdzinski, S.; Strehmel, V.; Sangoro, J. R.; Paluch, M. Effect of Pressure on Decoupling of Ionic Conductivity from Segmental Dynamics in Polymerized Ionic Liquids. *Macromolecules* **2015**, 48, 8660–8666.
19. Wojnarowska, Z.; Knapik, J.; Díaz, M.; Ortiz, A.; Ortiz, I.; Paluch, M. Conductivity Mechanism in Polymerized Imidazolium-Based Protic Ionic Liquid [HSO₃–BVIIm][OTf]: Dielectric Relaxation Studies. *Macromolecules* **2014**, 47, 4056–4065.
20. Choi, U.H.; Ye, Y.; Salas-de la Cruz, D.; Liu, W.; Winey, K. I.; Elabd, Y. A.; Runt, J.; Colby, R. H. Dielectric and Viscoelastic Responses of Imidazolium-Based Ionomers

- with Different Counterions and Side Chain Lengths. *Macromolecules* **2014**, 47, 777-790.
21. Allen, M. H.; Wang, S.; Hemp, S. T.; Chen, Y.; Madsen, L. A.; Winey, K. I.; Long, T. E. Hydroxyalkyl-Containing Imidazolium Homopolymers: Correlation of Structure with Conductivity. *Macromolecules* **2013**, 46, 3037–3045.
 22. Salas-de la Cruz, D.; Green, M. D.; Ye, Y.; Elabd, Y. A.; Long, T. E.; Winey, K. I. Correlating Backbone-to-backbone Distance to Ionic Conductivity in Amorphous Polymerized Ionic Liquids. *Journal of Polymer Science, Part B: Polymer Physics* **2012**, 50, 338-346.
 23. Nakamura, K.; Fukao, K.; Inoue, T. Dielectric Relaxation and Viscoelastic Behavior of Polymerized Ionic Liquids with Various Counteranions. *Macromolecules* **2012**, 45, 3850-3858.
 24. Green, M. D.; Salas-de la Cruz, D.; Ye, Y.; Layman, J. M.; Elabd, Y. A.; Winey, K. I.; Long, T.E. Alkyl-Substituted *N*-Vinylimidazolium Polymerized Ionic Liquids: Thermal Properties and Ionic Conductivities. *Macromol. Chem. Phys.* **2011**, 212, 2522–2528.
 25. Choi, U. H.; Mittal, A.; Price, T. L.; Gibson, H. W.; Runt, J.; Colby, R. H. Polymerized Ionic Liquids with Enhanced Static Dielectric Constants. *Macromolecules* **2013**, 46, 1175–1186.
 26. Choi, U. H.; Lee, M.; Wang, S.; Liu, W.; Winey, K.I.; Gibson, H.W.; Colby, R. H. Ionic Conduction and Dielectric Response of Poly(imidazolium acrylate) Ionomers. *Macromolecules* **2012**, 45, 3974-3985.
 27. Heres, M.; Cosby, T.; Mapesa, E. U.; Liu, H.; Berdzinski, S.; Strehmel, V.; Dadmun, M.; Paddison, S. J.; Sangoro, J. Ion Transport in Glassy Polymerized Ionic Liquids: Unraveling the Impact of the Molecular Structure. *Macromolecules* **2019**, 52, 88–95.

28. Frenzel, F.; Borchert, P.; Anton, A. M.; Strehmel, V.; Kremer, F. Charge transport and glassy dynamics in polymeric ionic liquids as reflected by their inter- and intramolecular interactions. *Soft Matter* **2019**, 15, 1605–1618.
29. Mogurampelly, S.; Keith, J. R.; Ganesan, V. Mechanisms Underlying Ion Transport in Polymerized Ionic Liquids. *J. Am. Chem. Soc.* **2017**, 139, 9511–9514.
30. Wojnarowska, Z.; Feng, H.; Fu, Y.; Cheng, S.; Carroll, B.; Kumar, R.; Novikov, V. N.; Kisliuk, A. M.; Saito, T.; Kang, N.; Mays, J. W.; Sokolov, A. P.; Bocharova, V. Effect of Chain Rigidity on the Decoupling of Ion Motion from Segmental Relaxation in Polymerized Ionic Liquids: Ambient and Elevated Pressure Studies. *Macromolecules* **2017**, 50, 6710–6721.
31. Fan, F.; Wang, W.; Holt, A. P.; Feng, H.; Uhrig, D.; Lu, X.; Hong, T.; Wang, Y.; Kang, N.; Mays, J.; Sokolov, A. P. Effect of Molecular Weight on the Ion Transport Mechanism in Polymerized Ionic Liquids. *Macromolecules* **2016**, 49, 4557–4570.
32. Fan, F.; Wang, Y.; Hong, T.; Heres, M. F.; Saito, T.; Sokolov, A. P. Ion Conduction in Polymerized Ionic Liquids with Different Pendant Groups. *Macromolecules* **2015**, 48, 4461–4470.
33. Keith, J. R.; Rebello, N. J.; Cowen, B. J.; Ganesan, V. Influence of Counterion Structure on Conductivity of Polymerized Ionic Liquids. *ACS Macro Lett.* **2019**, 8, 387–392.
34. Iacob, C.; Matsumoto, A.; Brennan, M.; Liu, H.; Paddison, S. J.; Urakawa, O.; Inoue, T.; Sangoro, J.; Runt, J. Polymerized Ionic Liquids: Correlation of Ionic Conductivity with Nanoscale Morphology and Counterion Volume. *ACS Macro Lett.* **2017**, 6, 941–946.
35. Stacy, E. W.; Gainaru, C. P.; Gobet, M.; Wojnarowska, Z.; Bocharova, V.; Greenbaum, S. G.; Sokolov, A. P. Fundamental Limitations of Ionic Conductivity in Polymerized Ionic Liquids. *Macromolecules* **2018**, 51, 8637–8645

36. Marcilla, R.; Blazquez, J. A.; Rodriguez, J.; Pomposo, J. A.; Mecerreyes, D. Tuning the Solubility of Polymerized Ionic Liquids by Simple Anion-Exchange Reactions. *J. Polym. Sci. A* **2004**, 42, 208-212.
37. Marcilla, R.; Blazquez, J. A.; Fernandez, R.; Grande, H.; Pomposo, J. A.; Mecerreyes, D. Synthesis of Novel Polycations Using the Chemistry of Ionic Liquids. *Macromol. Chem. Phys.* **2005**, 206, 299-304.
38. Matsumoto, A.; Iacob, C.; Noda, T.; Urakawa, O.; Runt, J.; Inoue, T. Introducing Large Counteranions Enhances the Elastic Modulus of Imidazolium-Based Polymerized Ionic Liquids. *Macromolecules* **2018**, 51, 4129-4142.
39. Kremer, F.; Schönhals, A. *Broadband Dielectric Spectroscopy*; Springer: Berlin, **2003**.
40. Wübbenhorst, M.; van Turnhout, J. Analysis of complex dielectric spectra. I. One-dimensional derivative techniques and three-dimensional modelling. *Journal of Non-Crystalline Solids* **2002**, 305, 40-49.
41. Boersma, A.; van Turnhout, J.; Wübbenhorst, M. Dielectric Characterization of a Thermotropic Liquid Crystalline Copolyesteramide: 1. Relaxation Peak Assignment. *Macromolecules* **1998**, 31, 7453-7460.
42. Díaz-Calleja, R. Comment on the Maximum in the Loss Permittivity for the Havriliak-Negami Equation. *Macromolecules* **2000**, 33, 8924.
43. Benassi, P.; Nardone, M.; Giugni, A.; Baldi, G.; Fontana, A. Collective excitations in liquid and glassy 3-methylpentane. *PHYSICAL REVIEW B* **2015**, 92, 104203.
44. Nakamura, K.; Saiwaki, T.; Fukao, K.; Inoue, T. Viscoelastic Behavior of the Polymerized Ionic Liquid Poly(1-ethyl-3-vinylimidazolium bis(trifluoromethanesulfonylimide)). *Macromolecules* **2011**, 44, 7719-7726.

45. Liu, H.; Paddison, S. J. Direct Comparison of Atomistic Molecular Dynamics Simulations and X-ray Scattering of Polymerized Ionic Liquids. *ACS Macro Lett.* **2016**, *5*, 537–543.
46. Pereiro, A. B.; Pastoriza-Gallego, M. J.; Shimizu, K.; Marrucho, I. M.; Canongia Lopes, J. N.; Piñeiro, M. M.; Rebelo, L. P. On the Formation of a Third, Nanostructured Domain in Ionic Liquids., *J. Phys. Chem. B*, **2013**, *117*, 10826-10833.
47. Ferreira, M. L.; Pastoriza-Gallego, M. J.; Araújo, J. M. M.; Canongia Lopes, J. N.; Rebelo, L. P. N.; Piñeiro, M. M.; Shimizu, K.; Pereiro, A. B. Influence of Nanosegregation on the Phase Behavior of Fluorinated Ionic Liquids. *J. Phys. Chem. C* **2017**, *121*, 5415–5427.
48. Tudryn, G.J.; Liu, W.; Wang, S.; Colby, R.H. Counterion Dynamics in Polyester-Sulfonate Ionomers with Ionic Liquid Counterions. *Macromolecules* **2011**, *44*, 3572-3582.
49. Kunal, K.; Robertson, C. G.; Pawlus, S.; Hahn, S. F.; Sokolov, A. P. Role of Chemical Structure in Fragility of Polymers: A Qualitative Picture. *Macromolecules* **2008**, *41*, 7232-7238.
50. Onsager, L. Electric Moments of Molecules in Liquids. *J. Am. Chem. Soc.* **1936**, *58*, 1486–1493.
51. Bartels, J.; Hess, A.; Shiau, H.; Allcock, H. R.; Colby, R. H.; Runt, J. Synthesis, Morphology, and Ion Conduction of Polyphosphazene Ammonium Iodide Ionomers. *Macromolecules* **2015**, *48*, 111-118.
52. Hu, H.; Yuan, W.; Lu, L.; Zhou, H.; Jia, Z.; Baker, G. L. Low glass transition temperature polymer electrolyte prepared from ionic liquid grafted polyethylene oxide. *Journal of Polymer Science, Part A: Polymer Chemistry* **2014**, *52*, 2104–2110.